applied sciences

MDPI

Article

Optical Vortex-Pumped $KTiOAsO_4$ Narrow-Linewidth Picosecond-Pulsed Parametric Oscillator

Xiazhuo Jiao [1], Jianqiang Ye [1], Mailikeguli Aihemaiti [1], Yuxia Zhou [1,2], Sujian Niu [1] and Xining Yang [1,*]

[1] Xinjiang Key Laboratory for Luminescence Minerals and Optical Functional Materials, School of Physics and Electronic Engineering, Xinjiang Normal University, Urumqi 830054, China; 15191037514@163.com (X.J.); a642226834@gmail.com (J.Y.); 18935930314@163.com (M.A.); zhou_yx0801@sina.com (Y.Z.); nsj@xjnu.edu.cn (S.N.)

[2] College of Chemistry and Chemical Engineering, Xinjiang Normal University, Urumqi 830054, China

* Correspondence: yangxn1984@126.com

Abstract: Herein, we present a picosecond-pulsed optical vortex parametric oscillator capable of generating high-power, narrow-linewidth near- and mid-infrared optical vortex outputs. The optical parametric oscillator (OPO), consisting of a $KTiOAsO_4$ (KTA) crystal and a Z-shaped standing wave cavity formed by five mirrors, transferred the orbital angular momentum (OAM) of the pump field to the signal and idler fields. The transmission mechanism of the OAM within the signal singly resonantsingly-resonant KTA-OPO was investigated, and the OAM was controlled and selectively transferred among the pump, signal, and idler fields by adjusting the focus position of the pump beam on the KTA crystal. With an incident pump power of 17 W, the maximum average output power was 2.14 W at 1535 nm (signal vortex field) and 0.95 W at 3468 nm (idler vortex field), respectively, corresponding to optical conversion efficiencies of 20.8% and 9.2%. The spectral linewidths of the signal and idler vortex fields were 0.502 nm and 1.216 nm, respectively. To the best of our knowledge, this is the first instance of a picosecond-pulsed optical vortex parametric oscillator with a KTA crystal.

Keywords: optical vortex; picosecond pulse; optical parametric oscillator; $KTiOAsO_4$ crystal; narrow linewidth

check for updates

Academic Editor: Detlef Kip

Received: 9 December 2024
Revised: 6 January 2025
Accepted: 7 January 2025
Published: 8 January 2025

Citation: Jiao, X.; Ye, J.; Aihemaiti, M.; Zhou, Y.; Niu, S.; Yang, X. Optical Vortex-Pumped $KTiOAsO_4$ Narrow-Linewidth Picosecond-Pulsed Parametric Oscillator. *Appl. Sci.* **2025**, *15*, 539. https://doi.org/10.3390/app15020539

Copyright: © 2025 by the authors. Licensee MDPI, Basel, Switzerland. This article is an open access article distributed under the terms and conditions of the Creative Commons Attribution (CC BY) license (https://creativecommons.org/licenses/by/4.0/).

1. Introduction

The orbital angular momentum (OAM) of light has been proven to be exceptionally valuable in quantum information [1,2], free-space telecommunications [3,4], optical trapping of trapped particles [5–7], materials processing [8], lithography [9], super-resolution microscopy [10–12], and the nano/microfabrication of helical structured materials [13–15], owing to an additional degree of freedom it offers. Optical vortex beams with a spiral phase wavefront have phase singularities and carry OAM. It can be characterized by an azimuthal phase term $\exp(i\ell\varphi)$, where ℓ indicates the topological charge or vortex order, and each photon in an optical vortex beam with ℓ holds an OAM of $\ell\hbar$ [16–18]. Nevertheless, to fully exploit the additional degree of freedom offered by the OAM and develop exciting new applications, several methods have been adopted to generate optical vortex beams, including astigmatic optical elements [16] and phase elements that modulate the wavefront of light, such as spiral phase plates (SPPs) [19], cylindrical lenses [20], spatial light modulators [21], and *Q*-plates [22]. Additionally, several techniques for directly generating vortex beams from laser systems have been developed, such as annular-shaped beam pumps [23], cavity mirrors with spot defects [24], intra-cavity phase-manipulating optical elements [25],

and off-axis pumping configurations [26]. However, these techniques are restricted to generating vortex laser beams within the visible and near-infrared wavelength range; thus, there is an urgent need for technologies that can extend the wavelength range.

To identify appropriate mode converters, nonlinear optics has been employed as an alternative approach to generate optical beams with diverse spatial structures. Optical parametric oscillation (OPO) is a second-order nonlinear process that has been widely utilized for laser frequency conversion [27,28]. On continuous wave and nanosecond pulse time scales, OPO has been utilized to generate optical vortex beams in the near- and mid-infrared regions [24,29,30]. In contrast, investigations into generating picosecond optical vortex beams have been seldom reported. Picosecond vortex lasers can be applied for the cold-etching effect to fabricate high-aspect-ratio chiral nanostructures, and narrow-linewidth mid-infrared picosecond vortex-pulsed lasers have considerable potential in the manufacturing of twisted organic materials, super-resolution molecular absorption microscopy, and super-resolution molecular spectroscopy [31]. In 2018 and 2022, Valen et al. reported that the OPOs using MgO-doped periodically polarized lithium tantalate/niobate (MgO:sPPLT and MgO:PPLN) crystals were capable of generating tunable picosecond-pulsed vortex laser beams with an order of ℓ = 1~5 within the mid-infrared wavelength range [32,33]. In 2024, our group successfully achieved wide-tunable (with a wavelength range of 1.3–5 μm) picosecond-pulsed vortex laser output with an order of ℓ = 1 by employing MgO:PPLN crystals [28]. Nevertheless, due to the broad acceptance angle in PPLN crystals, the spectral linewidths of the generated signal and idler fields were quite broad. For the aforementioned applications, it was obvious that narrow-linewidth picosecond-pulsed vortex laser sources were preferred. To date, we have verified that an optical vortex output with a narrower linewidth than that of the PPLN-OPO can be produced using a KTA-OPO pumped with a nanosecond optical vortex laser, which can be attributed to the narrower acceptance angle of the KTA [29,34,35].

In this paper, we propose a method for generating narrow-linewidth ultrafast vortex laser emission in the near- and mid-infrared wavelength regions using a 1064 nm picosecond optical vortex to pump a KTA-OPO. The selective transfer of the OAM of the pump field to the signal or idler fields was achieved by modifying the position of the pump beam focused on the KTA crystal. A maximum average output power of 2.14 W was attained at the signal vortex field, and at the idler vortex field, it was 0.95 W. The spectral linewidths of the signal and idler vortex fields were 0.502 nm and 1.216 nm, respectively. To the best of our knowledge, this is the narrowest linewidth obtained by picosecond vortex beam pumping an OPO. Our work indicates the significant potential of the KTA crystal in the field of narrow-linewidth picosecond vortex lasers in the near- and mid-infrared wavebands.

2. Experimental Setup

The experimental setup of this work is depicted in Figure 1a. An all-solid-state Nd:YVO_4 laser served as the pump source for the OPO with an output wavelength of 1064 nm, a pulse width of 15 ps, a pulse repetition frequency of 120 MHz, a maximum average output power of 18 W, and a near-Gaussian spatial output profile (M^2 < 1.3). A Faraday rotator (FR) was employed to eliminate the backward-reflected light and safeguard the Nd:YVO_4 laser from damage. The incident power of the OPO was regulated through the combined use of a half-wave plate (HWP) and a thin-film polarizer. The pump beam was transformed into a vortex beam using an SPP, which exhibits an annular spatial intensity profile as shown in Figure 1b. The topological charge characteristics of the generated vortex beam were determined with the tilted lens method, and the two lobes in the spatial intensity profile of the beam observed through the lens arrangement, as shown in Figure 1c, confirmed that the pump vortex beam has a topological charge of ℓ = 1.

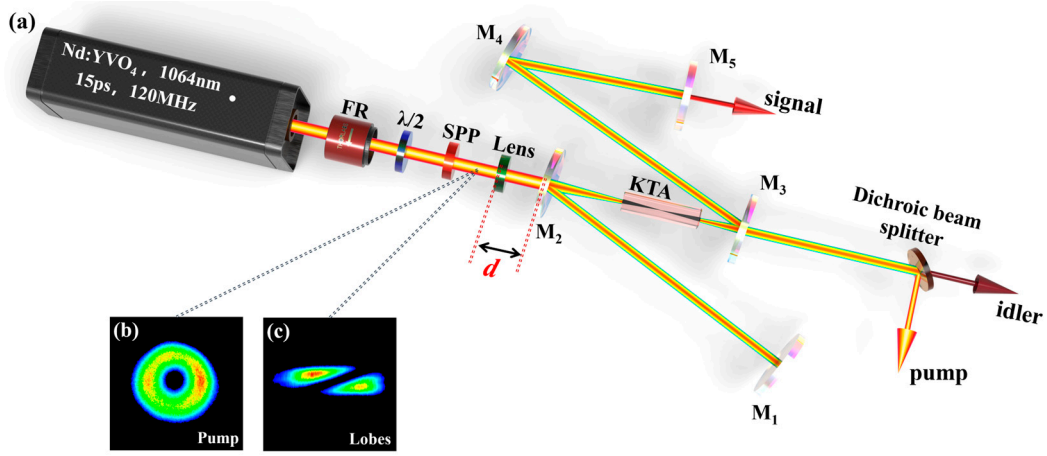


Figure 1. (**a**) Experimental configuration of the optical vortex-pumped KTA picosecond-pulsed parametric oscillator. λ/2, HWP; (**b**,**c**) show the spatial intensity profile of the pump vortex beam after the SPP conversion and when passing through a tilted lens.

The pump vortex beam was focused on the KTA crystal using a plano-convex lens with a focal length of 100 mm. The lens was installed on a high-precision translation stage that allowed the focal position of the pump vortex beam to be variable within the KTA crystal, thus altering the spatial overlap of the pump, signal, and idler fields. The KTA crystal, with a length of 30 mm and end faces sized 5 mm × 5 mm, was precisely cut to achieve type II non-critical phase matching (NCPM). Both of the end faces were coated with an anti-reflection film (reflectivity < 0.5%) to enhance transmission at wavelengths of 1064 nm (pump field), 1535 nm (signal field), and 3468 nm (idler field). The OPO was singly resonant for the signal field and was formed using five mirrors in a *Z*-shaped standing wave cavity configuration. M_2 (R = 150 mm) and M_3 (R = 150 mm) were plane-concave mirrors placed on either side of the KTA crystal, and the distance between them was 167 mm. A flat mirror M_1 and two plane-concave mirrors M_4 (R = 500 mm) and M_5 (R = 1000 mm) also contributed to the formation of the OPO cavity. Specifically, M_1–M_4 were high-reflection coated for the signal field (R > 99.9%) and anti-reflection coated for the pump and idler fields (R < 0.5%; R < 2%). M_5 was partially transmission coated for the signal field (R = 80%) to ensure resonance of the signal field. M_1 was firmly attached to a high-precision translation stage for precisely adjusting the cavity length of the OPO and attaining synchronization with the pump laser. The total round-trip optical path length of the OPO cavity amounted to 1250 mm. Additionally, a dichroic beam splitter was utilized to separate the co-propagating idler field from the remaining pump field. The output power and spatial intensity profiles of the signal field and idle field were measured with a power meter and a Spiricon pyroelectric camera III (Ophir-Spiricon, North Logan, UT, USA).

3. Results and Discussion

3.1. Modes of the Output Beam

Generally, there are two methods for determining the order of the output optical vortex. One is that when an optical vortex beam of order ℓ passes through a tilted lens, it will be transformed into a multi-lobed beam with $\ell + 1$ lobes [36]. The other is that when an optical vortex beam of order ℓ passes through a Mach–Zehnder interferometer, it will be transformed into a pair of forked fringes with a $\ell + 1$ leg structure oriented in opposite directions [37]. Based on this, the beam output mode can be ascertained. As depicted in Figure 2, the spatial intensity profiles and the profiles of the output signal and idler fields are presented for different focus positions of the pump vortex beam when passing through a Mach–Zehnder interferometer or a tilted lens. Notably, *d* denotes the distance between

the pump beam focusing lens and M_2. By adjusting the position of the focusing lens, d was set to 43 cm, 45 cm, and 47 cm. Under these conditions, the focal point of the pump vortex beam was positioned at the front, middle, and rear of the KTA crystal, respectively.

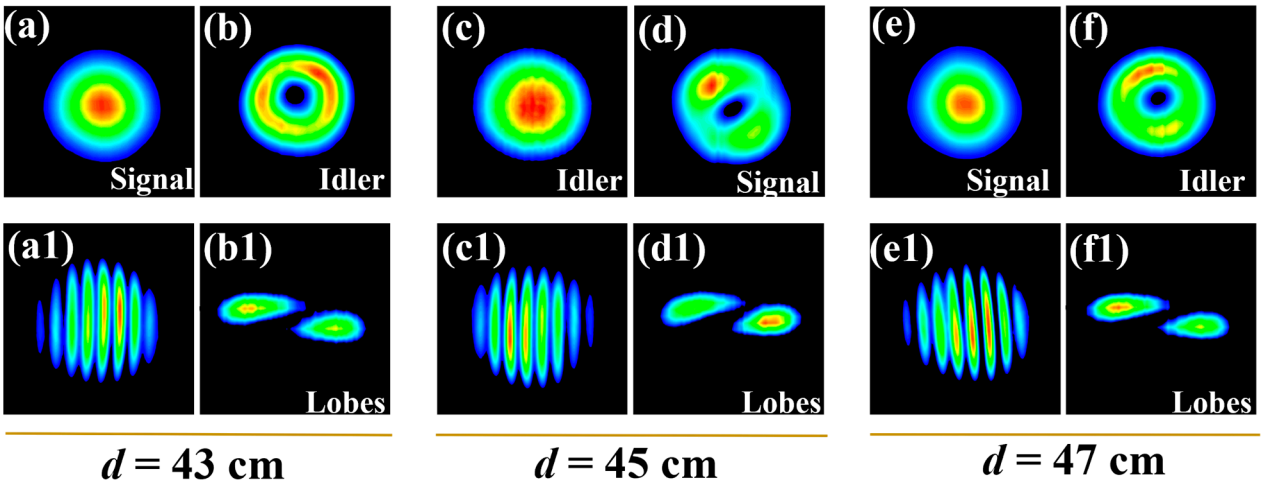


Figure 2. Images (**a**–**f**) depicting the spatial intensity profiles of the signal and idler beams as generated from the KTA-OPO for a variety of pump beam focal positions; images (**a1**–**f1**) showing the corresponding spatial intensity profiles of the signal and idler beams as generated when employing a Mach–Zehnder interferometer or a tilted lens.

Figure 2a,b reveal that the intensity profile of the output signal field was Gaussian, while that of the idler field was annular, respectively, when the pump vortex beam was focused on the front face of the crystal (d = 43 mm, and the pump beam radius here was measured to be 146 μm). As shown in Figure 2a1, when the signal field was characterized using the Mach–Zehnder interference technique, a series of fringes were generated. The straight-line fringes, a characteristic pattern for the plane phase front, signified that the resonant signal beam was output in a Gaussian mode. When the idler field was analyzed with the tilted lens method, two lobes were produced, as observed in Figure 2(b1), confirming that the order of the idler field was ℓ_i = 1, which was the same as that of the pump vortex field. These findings suggest that the OAM of the pump field was transferred to the idler field.

When the focus of the pump vortex was located at the center of the KTA crystal (d = 45 mm, and the pump beam radius here was measured to be 90 μm), the generated signal and idler fields exhibited distinct spatial profiles. In this situation, the idler field possessed a Gaussian spatial intensity profile (Figure 2c), whereas the signal field had an annular spatial intensity profile (Figure 2d). The Mach–Zehnder and tilted lens characterizations were also applied to these outputs, and the resulting spatial intensity profiles were displayed in Figure 2(c1) and Figure 2(d1), respectively. It can be analyzed that the OAM of the pumping field has been transferred to the signal field.

When the pump vortex beam was focused on the end face of the KTA crystal (d = 47 mm, and the pump beam radius here was measured to be 153 μm), the spatial intensity profiles of the generated signal and idler fields were similar to those when the pump beam was focused on the front surface of the KTA crystal. The signal field featured a Gaussian spatial intensity profile (Figure 2e), while the idler field exhibited an annular spatial intensity profile (Figure 2f). The spatial intensity profiles of these beams when passing through the Mach–Zehnder and tilted lens setups are, respectively, presented in Figure 2(e1),(f1). In this case, the OAM of the pump field was transferred to the idler field.

These results indicate that by adjusting the focal position of the pump field within the KTA crystal, the OAM of the pump field can be selectively imparted to either the signal

or idler fields. KTA crystals, which exhibit NCPM, have garnered significant attention in research due to their large nonlinear coefficient (d_{24} = 3.43 pm/V), wide acceptance angle, and the absence of walk-off effects during nonlinear frequency conversion [38]. However, in ultrafast high-order vortex beam-pumped applications, KTA crystals require a higher oscillation threshold compared to MgO:PPLN crystals that utilize quasi-phase matching. Consequently, achieving high-order vortex laser sources and generating complex near- to mid-infrared vortex beams necessitates the use of pump sources with significantly higher peak power [29,32,39]. To offer a better explanation of this phenomenon, we conducted a theoretical analysis of the spatial overlap changes between the pump, signal, and idler fields within the OPO.

3.2. Spatial Overlap Efficiency

Previous efforts have confirmed that due to the conservation of OAM within an OPO cavity, the transfer of OAM among the pump, signal, and idler fields can be regulated by modulating cavity losses or by modifying the spatial overlap of respective fields [40]. Generally, in ultrafast OPOs, a cavity design capable of synchronizing with a high-repetition-rate pump field is necessary. Z-shaped or ring-shaped cavities and a large number of mirrors with various curvature radii are typically employed. This may result in a resonant field with significant astigmatism and diffraction losses, causing the resonant field to oscillate in Gaussian mode, while the non-resonant field possesses the OAM characteristics of the pump field [41]. The closer the overlap of the pump field as any one mode of space approaches 1, the lower the loss, and the more readily the cavity oscillates in that mode. In this study, we adjusted the spatial overlap efficiency between the pump and parametric field to precisely control the transfer of the pump field's OAM. The formula for the spatial intensity overlap efficiency (η) between the pump and parametric field within the KTA crystal is presented below, as derived from reference [42]:

$$\eta = \frac{\left| \iint E_p(r,\varphi) E_{s,i}^*(r,\varphi) r dr d\varphi \right|^2}{\iint \left| E_p(r,\varphi) \right|^2 r dr d\varphi * \iint \left| E_{s,i}(r,\varphi) \right|^2 r dr d\varphi} \quad (1)$$

where E_p represents the electric field of the pump field, E_s represents the electric field of the signal field, and E_i represents the electric field of the idler field. The pump, idler, and signal fields are assumed to lase with a vortex mode (ℓ = 1) within the cavity, which can be expressed as

$$E_{p,s,i} = \frac{1}{\omega_{0_{p,s,i}}} * \frac{\sqrt{2}r}{\omega_{p,s,i}} * exp\left(-\frac{r^2}{\omega_{p,s,i}^2} \right) exp(i\varphi) \quad (2)$$

where $\omega_{p,s,i}$ is the pump, signal, or idler beam radius, and $\omega_{0p,s,i}$ is the fundamental mode size of the pump, signal, or idler field.

In this theoretical model, the mode sizes of the signal (ω_s = 92 μm) and idler fields (ω_i = 180 μm), which were assumed to be fixed, at the center of the KTA crystal were determined based on the parameters of the OPO cavity mirrors using the ABCD resonator model. Subsequently, the spatial overlap efficiency between the pump field and the signal or idler fields as a function of the pump beam radius (ω_p) was calculated and is presented in Figure 3. It can be observed that when the pump beam radius ranged from 80 to 120 μm; the spatial overlap between the first-order vortex mode (LG_{01}) of the signal field and the pump field was higher compared to other modes, thereby reducing cavity loss and enabling the signal beam to oscillate in the vortex mode. As the pump spot size gradually increased (ω_p > 142 μm), the spatial overlap between the first-order signal beam and the pump beam deteriorated, leading to increased diffraction loss within the cavity and forcing the signal beam to oscillate in the Gaussian (GS) mode. Due to the conservation of OAM

and the improved spatial overlap between the LG_{01} of the idler beam and the pump beam, the pump beam transferred the OAM to the idler field output.

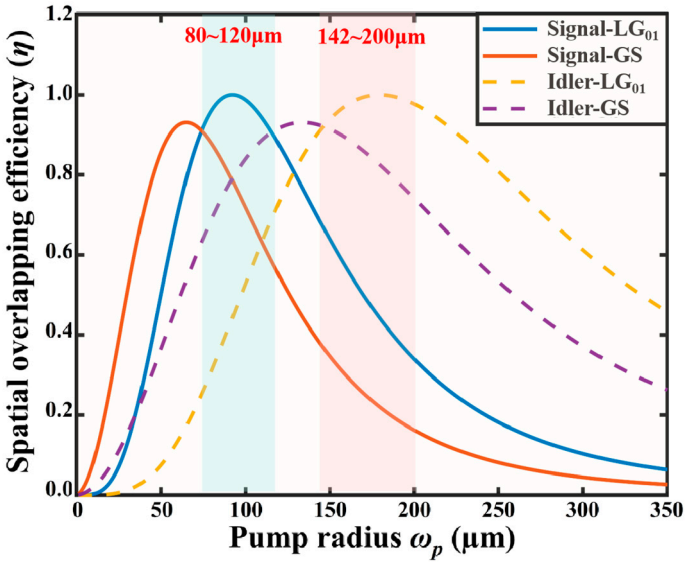


Figure 3. Plot showing the spatial overlap efficiency between the pump field and the signal or idler fields as a function of the pump beam radius (ω_p).

In the experiment, we utilized a focusing lens with a focal length of 100 mm to focus the pump beam of the vortex mode to a minimum spot size of 89.7 μm. When d was set to 45 mm, the signal beam was generated in the vortex mode, while the idler beam was emitted in the Gaussian mode. For d = 43 mm or d = 47 mm, the pump beam radius at the crystal increased (ω_p > 142 μm), resulting in the idler beam acquiring OAM from the pump beam and the signal beam being emitted in the fundamental mode. When ω_p exceeded 200 μm, the peak power density within the cavity failed to reach the oscillation threshold, causing the OPO resonator to cease oscillation.

These theoretical simulation results support the experimental findings that selective OAM transfer can be achieved simply by regulating the size of the pump field relative to the resonant field mode size of a given cavity design. This correlation not only validates the theoretical predictions but also serves as a practical guideline for experimental setups. This also contributes to the explanation of why a large number of picosecond vortex-pumped OPOs tend to generate optical vortex outputs (typically non-resonant secondary fields) in the mid-infrared wavelength range without employing additional optical components to reduce intracavity loss. Understanding this phenomenon is crucial for advancing the field of OAM-based photonics and developing novel applications in optical communication, imaging, sensing, etc.

3.3. Output Performance of Laser Vortices

The beam quality factor M^2 of the vortex idler field generated in this research was precisely measured by employing the knife-edge method, considering both the calculated beam diameter at the resonator focus and the measured beam diameter in the far field to determine the divergence of the idler beam. Figure 4a depicts the variation in the beam size as a function of position through the focus of a f = 150 mm lens for the idler field. The beam quality factors in the two orthogonal directions were M_x^2 = 2.46 and M_y^2 = 2.25, respectively, indicating that the beam shape of the output picosecond-pulsed idler optical vortex approaches the ideal beam quality of an optical vortex with ℓ_i = 1.

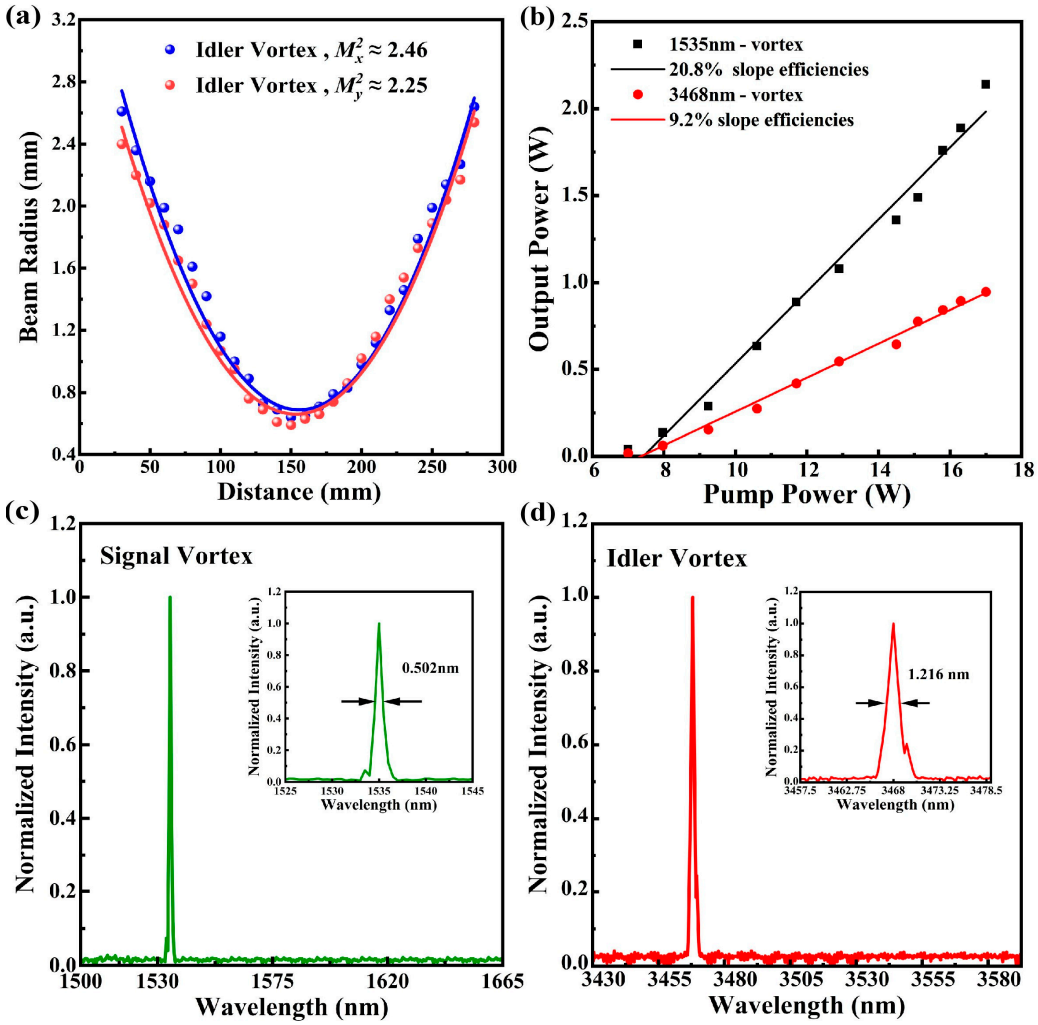


Figure 4. (**a**) The beam quality of the output idler vortex; (**b**) the output power of the signal and idler vortices; (**c**,**d**) the spectral of the output signal and idler vortices. Insets show the spectral bandwidths of the output signal and idler vortices, respectively.

The average output powers of the signal and idler fields in relation to the average pump power are presented in Figure 4b. Here, the maximum vortex output powers of the signal and idler fields were 2.14 W and 0.95 W, respectively, when the pump power was 17 W. Optical slope efficiencies of 20.8% and 9.2% were achieved for the signal and idler fields, respectively. In ultrafast OPOs, the transmittance of the output mirror has a significant impact on the overall system output power [43]. It was discovered throughout our work that an output mirror with 20% transmittance for the resonant signal field provided the optimal balance of a high signal and idler field output from the OPO while maintaining a relatively low oscillation threshold.

The spectral characteristics of the signal and idler fields are shown in Figures 4c and 4d, respectively. The spectra were recorded using a scanning monochromator (SpectraPro HRS-500, PI, Trenton, NJ, USA) with 300 lines/mm, an aperture size of 30 μm, and a spectral resolution of 0.1–0.2 nm. The KTA crystal that complies with the NCPM can only output signal and idler fields of fixed wavelengths. The central output wavelength of the signal vortex field was located at 1535 nm in the near-infrared band, and the central output wavelength of the idler vortex field was placed at 3468 nm in the mid-infrared band. The full width at half maxima (FWHM) of the signal vortex and idler vortex outputs were measured to be $\Delta\lambda_s$ = 0.502 nm and $\Delta\lambda_i$ = 1.216 nm, respectively. Compared with a MgO:PPLN-OPO, the KTA-OPO in this work has lower temperature sensitivity and a

narrower spectral acceptance angle, which results in narrower spectral linewidths and better monochromaticity of the output signal and idler fields [31].

4. Conclusions

In conclusion, we demonstrated a picosecond, narrow-linewidth, and fixed-wavelength vortex source that generated emissions in the near- and mid-infrared wavelength range from a KTA-OPO. We experimentally verified the controlled transfer of OAM from an incident pump field to either the signal or idler fields by changing the focal position of the pump field within the KTA crystal. The mechanism of OAM transfer was theoretically modeled by analyzing the spatial overlap factor between the incident pump field and the resonant mode of the OPO. At a pump power of 17 W, the maximum signal and idler vortex output powers were measured as 2.14 W and 0.95 W, corresponding to slope efficiencies of 20.8% and 9.2%, respectively. The FWHM of the signal and idler vortex outputs was also measured to be $\Delta\lambda_s$ = 0.502 nm and $\Delta\lambda_i$ = 1.216 nm, respectively. This indicates that narrow-linewidth optical vortex laser outputs can be generated in the ultrafast, picosecond-pulse regime using KTA crystals.

Author Contributions: Conceptualization, X.J., Y.Z. and X.Y.; methodology, X.J. and M.A.; software, X.J. and J.Y.; validation, X.Y. and S.N.; formal analysis, X.J.; investigation, X.J., Y.Z. and X.Y.; resources, X.Y.; data curation, X.J. and Y.Z.; writing—original draft preparation, X.J.; writing—review and editing, X.Y., Y.Z. and S.N.; supervision, X.Y.; project administration, S.N.; funding acquisition, X.Y. All authors have read and agreed to the published version of the manuscript.

Funding: This work was supported by the Natural Science Foundation of Xinjiang Uygur Autonomous Region (2022D01A221), the Postdoctoral Science Foundation of China (2021MD703833), the Ministry of Education's Industry-University Cooperation and Collaborative Education Program (23110409093007), the Postdoctoral Foundation of Heilongjiang Province (LBH-Z21206), and the Talent Development Fund "Tianchi Talents" Introduction Program of Xinjiang Uygur Autonomous Region.

Institutional Review Board Statement: Not applicable.

Informed Consent Statement: Not applicable.

Data Availability Statement: The raw data supporting the conclusions of this article will be made available by the authors on request.

Conflicts of Interest: The authors declare no conflicts of interest.

References

1. Sit, A.; Bouchard, F.; Fickler, R.; Gagnon-Bischoff, J.; Larocque, H.; Heshami, K.; Elser, D.; Peuntinger, C.; Günthner, K.; Heim, B.; et al. High-dimensional Intracity Quantum Cryptography with Structured Photons. *Optica* **2017**, *4*, 1006–1010. [CrossRef]
2. Mair, A.; Vaziri, A.; Weihs, G.; Zeilinger, A. Entanglement of the Orbital Angular Momentum States of Photons. *Nature* **2001**, *412*, 313–316. [CrossRef] [PubMed]
3. Wang, J.; Yang, J.Y.; Fazal, I.M.; Ahmed, N.; Yan, Y.; Huang, H.; Ren, Y.; Yue, Y.; Dolinar, S.; Tur, M.; et al. Terabit Free-space Data Transmission Employing Orbital Angular Momentum Multiplexing. *Nat. Photonics* **2012**, *6*, 488–496. [CrossRef]
4. Xia, T.; Xie, Z.; Yuan, X. Multidimensional Multiplexing Holography Based on Optical Orbital Angular Momentum Lattice Multiplexing. *Adv. Photonics Nexus* **2024**, *3*, 016005. [CrossRef]
5. Ng, J.; Lin, Z.; Chan, C.T. Theory of Optical Trapping by an Optical Vortex Beam. *Phys. Rev. Lett.* **2010**, *104*, 103601. [CrossRef] [PubMed]
6. Grier, D.G. A Revolution in Optical Manipulation. *Nature* **2003**, *424*, 810–816. [CrossRef]
7. Wang, Y.; Shen, Y.; Meng, Y.; Gong, M. Generation of 1535-nm Pulsed Vortex Beam in a Diode-pumped Er,Yb: Glass Microchip Laser. *IEEE Photonics Tech. L* **2018**, *30*, 891–894. [CrossRef]
8. Hnatovsky, C.; Shvedov, V.G.; Krolikowski, W.; Rode, A.V. Materials Processing with a Tightly Focused Femtosecond Laser Vortex Pulse. *Opt. Let.* **2010**, *35*, 3417–3419. [CrossRef] [PubMed]

9. Allegre, O.J.; Jin, Y.; Perrie, W.; Ouyang, J.; Fearon, E.; Edwardson, S.P.; Dearden, G. Complete Wavefront and Polarization Control for Ultrashort-pulse Laser Microprocessing. *Opt. Express* **2013**, *21*, 21198–21207. [CrossRef] [PubMed]
10. Bretschneider, S.; Eggeling, C.; Hell, S.W. Breaking the Diffraction Barrier in Fluorescence Microscopy by Optical Shelving. *Phys. Rev. Lett.* **2007**, *98*, 218103. [CrossRef] [PubMed]
11. Tamburini, F.; Anzolin, G.; Umbriaco, G.; Bianchini, A.; Barbieri, C. Overcoming the Rayleigh Criterion Limit with Optical Vortices. *Phys. Rev. Lett.* **2006**, *97*, 163903. [CrossRef] [PubMed]
12. Kozawa, Y.; Matsunaga, D.; Sato, S. Superresolution Imaging via Superoscillation Focusing of a Radially Polarized Beam. *Optica* **2018**, *5*, 86–92. [CrossRef]
13. Ni, J.; Wang, C.; Zhang, C.; Hu, Y.; Yang, L.; Lao, Z.; Xu, B.; Li, J.; Wu, D.; Chu, J. Three-dimensional Chiral Microstructures Fabricated by Structured Optical Vortices in Isotropic Material. *Light Sci. Appl.* **2017**, *6*, e17011. [CrossRef]
14. Omatsu, T.; Miyamoto, K.; Toyoda, K.; Morita, R.; Arita, Y.; Dholakia, K. Twisted Materials: A New Twist for Materials Science: The Formation of Chiral Structures using the Angular Momentum of Light. *Adv. Opt. Mater.* **2019**, *7*, 1970052. [CrossRef]
15. Syubaev, S.; Zhizhchenko, A.; Vitrik, O.; Porfirev, A.; Fomchenkov, S.; Khonina, S.; Kudryashov, S.; Kuchmizhak, A. Chirality of Laser-printed Plasmonic Nanoneedles Tunable by Tailoring Spiral-shape Pulses. *Appl. Surf. Sci.* **2019**, *470*, 526–534. [CrossRef]
16. Allen, L.; Beijersbergen, M.W.; Spreeuw, R.J.C.; Woerdman, J.P. Orbital Angular Momentum of Light and the Transformation of Laguerre-Gaussian Laser Modes. *Phys. Rev. A* **1992**, *45*, 8185. [CrossRef]
17. Yao, A.M.; Padgett, M.J. Orbital Angular Momentum: Origins, Behavior and Applications. *Adv. Opt. Photon.* **2011**, *3*, 161–204. [CrossRef]
18. Shen, Y.; Wang, X.; Xie, Z.; Min, C.; Fu, X.; Liu, Q.; Gong, M.; Yuan, X. Optical Vortices 30 Years on: OAM Manipulation from Topological Charge to Multiple Singularities. *Light. Sci. Appl.* **2019**, *8*, 90. [CrossRef] [PubMed]
19. Oemrawsingh, S.S.R.; Van Houwelingen, J.A.W.; Eliel, E.R.; Woerdman, J.P.; Verstegen, E.J.K.; Kloosterboer, J.G.; Hooft, G.W. Production and Characterization of Spiral Phase Plates for Optical Wavelengths. *Appl. Opt.* **2004**, *43*, 688–694. [CrossRef] [PubMed]
20. Beijersbergen, M.W.; Allen, L.; van der Veen, H.E.L.O.; Woerdman, J.P. Astigmatic Laser Mode Converters and Transfer of Orbital Angular Momentum. *Opt. Commun.* **1993**, *96*, 123–132. [CrossRef]
21. Heckenberg, N.R.; McDuff, R.; Smith, C.P.; White, A.G. Generation of Optical Phase Singularities by Computer-generated Holograms. *Opt. Lett.* **1992**, *17*, 221–223. [CrossRef] [PubMed]
22. Marrucci, L.; Manzo, C.; Paparo, D. Optical Spin-to-orbital Angular Momentum Conversion in Inhomogeneous Anisotropic Media. *Phys. Rev. Lett.* **2006**, *96*, 163905. [CrossRef] [PubMed]
23. Kim, J.W.; Clarkson, W.A. Selective Generation of Laguerre–Gaussian (LG_{0n}) Mode Output in a Diode-laser Pumped Nd: YAG Laser. *Opt. Commun.* **2013**, *296*, 109–112. [CrossRef]
24. Aadhi, A.; Sharma, V.; Samanta, G.K. High-power, continuous-wave, tunable mid-IR, higher-order vortex beam optical parametric oscillator. *Opt. Lett.* **2018**, *43*, 2312–2315. [CrossRef] [PubMed]
25. Sharma, V.; Kumar, S.C.; Samanta, G.K.; Ebrahim-Zadeh, M. Tunable Vortex Beam Generation Using an Optical Parametric Oscillator with an Antiresonant-ring Interferometer. *Opt. Lett.* **2021**, *46*, 3235–3238. [CrossRef] [PubMed]
26. Tuan, P.H.; Liang, H.C.; Huang, K.F.; Chen, Y. Realizing High-pulse-energy Large-angular-momentum Beams by Astigmatic Transformation of Geometric Modes in an Nd: YAG/Cr^{4+}:YAG Laser. *IEEE J. Sel. Top. Quantum Electron.* **2018**, *24*, 2798999. [CrossRef]
27. Jashaner, D.; Zhou, Y.; Yusufu, T. Widely-tunable Mid-infrared (2.6–5 μm) Picosecond Vortex Laser. *Appl. Phys. Exp.* **2022**, *15*, 102004. [CrossRef]
28. Aihemaiti, M.; Sulaiman, D.; Jashaner, D.; Zhou, Y.; Yang, X.; Li, Z.; Muhutijiang, B.; Yusufu, T. Tunable Near and Mid-Infrared (1.3–5 μm) Picosecond Pulsed Optical Vortex Parametric Oscillator. *Photonics* **2024**, *11*, 319. [CrossRef]
29. Mairihaba, M.; Wang, S.; Aierken, P.; Omatsu, T.; Yusufu, T. Near and Mid-infrared Optical Vortex Parametric Oscillator Based on KTA. *Sci. Rep.* **2021**, *1*, 8013. [CrossRef]
30. Aadhi, A.; Sharma, V.; Singh, R.P.; Samanta, G.K. Continuous-wave, Singly Resonant Parametric Oscillator-based Mid-infrared Optical Vortex Source. *Opt. Lett.* **2017**, *42*, 3674–3677. [CrossRef] [PubMed]
31. Masuda, K.; Shinozaki, R.; Shiraishi, A.; Ichijo, M.; Yamane, K.; Miyamoto, K.; Omatsu, T. Picosecond Optical Vortex-induced Chiral Surface Relief in an Azo-polymer film. *J. Nanophotonics* **2020**, *14*, 016012. [CrossRef]
32. Sharma, V.; Kumar, S.C.; Samanta, G.K.; Ebrahim-Zadeh, M. Orbital Angular Momentum Exchange in a Picosecond Optical Parametric Oscillator. *Opt. Lett.* **2018**, *43*, 3606–3609. [CrossRef] [PubMed]
33. Sharma, V.; Chaitanya Kumar, S.; Samanta, G.K.; Ebrahim-Zadeh, M. Tunable, High-power, High-order Optical Vortex Beam Generation in the Mid-infrared. *Opt. Exp.* **2022**, *30*, 1195–1204. [CrossRef] [PubMed]
34. Zhou, Y.; Yusufu, T.; Ma, Y.; Omatsu, T. Generation of Tunable, Non-integer OAM States From an Optical Parametric Oscillator. *Appl. Phys. Lett.* **2023**, *122*, e0141377. [CrossRef]

35. Zhou, Y.; Yang, X.; Ye, J.; Ma, Y.; Wan, Y.; Wen, J.; Yusufu, T. Generation of Tunable High-order Laguerre–Gaussian Petal-like Modes from a Mid-infrared Optical Vortex Parametric Oscillator. *Adv. Photonics Nexus* **2024**, *3*, 036013. [CrossRef]
36. Kotlyar, V.V.; Kovalev, A.A.; Porfirev, A.P. Astigmatic Transforms of an Optical Vortex for Measurement of its Topological Charge. *Appl. Opt.* **2017**, *56*, 4095–4104. [CrossRef]
37. Huang, H.; Ren, Y.; Yan, Y.; Ahmed, N.; Yue, Y.; Bozovich, A.; Erkmen, B.I.; Birnbaum, K.; Dolinar, S.; Tur, M.; et al. Phase-shift Interference-based Wavefront Characterization for Orbital Angular Momentum Modes. *Opt. Lett.* **2013**, *38*, 2348–2350. [CrossRef]
38. Cheng, L.K.; Cheng, L.T.; Bierlein, J.D.; Zumsteg, F.C.; Ballman, A.A. Properties of doped and undoped crystals of single domain $KTiOAsO_4$. *Appl. Phys. Lett.* **1993**, *62*, 346–348. [CrossRef]
39. Abulikemu, A.; Yakufu, S.; Zhou, Y.X.; Yusufu, T. Mid-infrared idler-resonant optical vortex parametric oscillator based on MgO: PPLN. *Opt. Laser Technol.* **2024**, *171*, 110341. [CrossRef]
40. Yusufu, T.; Niu, S.; Tuersun, P.; Tulake, Y.; Miyamoto, K.; Omatsu, T. Tunable 3 μm Optical Vortex Parametric Oscillator. *Jpn. J. Appl. Phys.* **2018**, *57*, 122701. [CrossRef]
41. Martinelli, M.; Huguenin, J.A.O.; Nussenzveig, P.; Khoury, A.Z. Orbital Angular Momentum Exchange in an Optical Parametric Oscillator. *Phys. Rev. A* **2004**, *70*, 013812. [CrossRef]
42. Yariv, A.; Yeh, P.; Yariv, A. *Photonics: Optical Electronics in Modern Communications*, 6th ed.; Oxford University Press: New York, NY, USA, 2007; pp. 204–210.
43. Ruffing, B.; Nebel, A.; Wallenstein, R. All-solid-state CW Mode-locked Picosecond $KTiOAsO_4$ (KTA) Optical Parametric Oscillator. *Appl. Phys. B* **1998**, *67*, 537–544. [CrossRef]

Disclaimer/Publisher's Note: The statements, opinions and data contained in all publications are solely those of the individual author(s) and contributor(s) and not of MDPI and/or the editor(s). MDPI and/or the editor(s) disclaim responsibility for any injury to people or property resulting from any ideas, methods, instructions or products referred to in the content.